Multimode quantum properties of a self-imaging optical parametric oscillator: Squeezed vacuum and Einstein-Podolsky-Rosen-beams generation

L. Lopez,[1] B. Chalopin,[1] A. Rivière de la Souchère,[1] C. Fabre,[1] A. Maître,[1,2] and N. Treps[1,*]
[1]*Laboratoire Kastler Brossel, Université Pierre et Marie Curie-Paris 6, ENS, CNRS, 4 Place Jussieu, 75005 Paris, France*
[2]*Institut des NanoSciences de Paris, Université Pierre et Marie Curie-Paris 6, Campus Boucicaut, 140 rue de Lourmel, 75015 Paris, France*

(Received 26 December 2008; published 16 October 2009)

We investigate the spatial quantum properties of the light emitted by a perfectly spatially degenerate optical parametric oscillator (self-imaging optical parametric oscillator). We show that this device produces local squeezing for areas bigger than a coherence area that depends on the crystal length and pump width. Furthermore, it generates local EPR beams in the far field. We show, calculating the eigenmodes of the system, that it is highly multimode for realistic experimental parameters.

DOI: 10.1103/PhysRevA.80.043816 PACS number(s): 42.50.Dv, 42.65.Yj, 42.60.Da

I. INTRODUCTION

Highly multiplexed quantum channels are more and more needed as complexity increases in the quantum communication and information protocols. They can be obtained by coupling many single mode quantum channels [1] but also by directly using highly multimode quantum systems. In addition, the resolution of several problems in quantum imaging [2] requires the generation of nonclassical states of light having adjustable shapes in the transverse plane: this is the case for super-resolution [3] or for image processing below the standard quantum noise level [4]. For all these reasons, it is very important to develop a source of highly multimode nonclassical light (squeezed and/or entangled) of arbitrary transverse shape.

In the continuous variable regime, where optical resonators are necessary to efficiently produce nonclassical states, one of the keys to successfully generate multimode light is the ability to operate a multimode optical resonator. Indeed, many theoretical proposals rely on the use of an optical parametric oscillator (OPO) operated below threshold with planar cavities [5] or with confocal cavities [6–8], which spatially filter half of the transverse modes. These proposals predict the generation of local vacuum squeezing and image amplification on modes that respect the cavity symmetry only. We propose here to keep the parametric process to generate nonclassical light and to use a fully transverse cavity, the self-imaging cavity [9]. This type of resonator used, for instance, to improve the power of multimode lasers [10], is in principle able to transmit any optical image within its spatial bandwidth.

The aim of this paper is to demonstrate that the self-imaging OPO is an excellent candidate to produce local squeezing, image amplification, and also local EPR beams, taking into account its physical limitations such as the thickness of the crystal and the finite size of the various optical beams and detectors. By extension, as in any type of degenerate OPO under the oscillation threshold, local squeezing is linked to local phase-sensitive amplification and therefore image amplification of any transverse shape.

The following section (Sec. II) describes the experimental configuration and develops the theoretical model, as well as the method used to determine the squeezing spectra measured in well-defined homodyne detection schemes. In Sec. III, the results for such quantities, respectively, in the near field and in the far field are given, and we investigate the generation of EPR beams. Finally, in Sec. IV, we compute the eigenmodes of the system and show that they are close to Hermite-Gauss modes.

II. SELF-IMAGING OPTICAL PARAMETRIC OSCILLATOR

A. Self-imaging cavity

We consider the parametric down conversion taking place in a self-imaging optical parametric oscillator whose cavity was depicted in the pioneer article of Arnaud [9]. Such a cavity is a fully transverse degenerate one, which implies that all the transverse modes of same frequency resonate for the same cavity length. From a geometrical point of view, an optical cavity is self-imaging when an arbitrary ray retraces its own path after a single round trip. The simplest self-imaging ring cavity requires three lenses of focal length f_i, $i=1,2,3$ [9]. As depicted in Fig. 1, the ring cavity is self-imaging provided the distances c_{ij} of the image plane of the lens i and the object plane of the lens j are given by

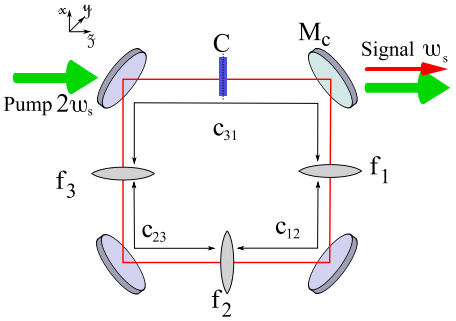

FIG. 1. (Color online) Self-imaging OPO scheme in a ring cavity configuration.

*treps@spectro.jussieu.fr

$$c_{12}=\frac{f_1 f_2}{f_3}, c_{23}=\frac{f_2 f_3}{f_1}, c_{31}=\frac{f_3 f_1}{f_2}. \quad (1)$$

Let us consider an OPO whose cavity is the self-imaging one described in Fig. 1 [9]. A type I parametric medium of length l_c is centered on the plane C located at the longitudinal coordinate $z=0$. The OPO is pumped by a Gaussian TEM_{00} field E_p of amplitude A_p and frequency $\omega_p=2\omega_s$. Its waist w_p is located at the plane C. The OPO works in a longitudinal degenerate operation for which signal and idler have the same frequency ω_s. We assume that for the pump wave, all the mirrors are totally transparent and that for the signal field, the coupling mirror M_c has a small transmission t; the other three mirrors being perfectly reflecting.

B. Electric field operator

We will follow an operator-based approach [11] close to the one developed in the confocal case [12], and in order to keep the present paper concise we give only the main steps of the calculation, as well as the improvement. The intracavity signal field at frequency ω_s is described by a field envelope operator $B(\mathbf{x},z)$. In the self-imaging resonator, at resonance, the field can be decomposed on any transverse-mode basis (such as the Gauss-Laguerre modes, for instance). The field operator becomes

$$\hat{B}(\mathbf{x},z,t)=\sum_l f_l(\mathbf{x},z)\hat{a}_l(z,t), \quad (2)$$

where $\hat{a}_l(z,t)$ is the annihilation operator of a photon in mode l at the cavity position z and at time t. f_l is the amplitude of the l mode. This field obeys the standard equal-time commutation relation at a given transverse plane at position z

$$[\hat{B}(\mathbf{x},z,t),\hat{B}^{\dagger}(\mathbf{x}',z,t)]=\delta(\mathbf{x}-\mathbf{x}'). \quad (3)$$

Indeed, contrary to the confocal case [12] or to any partially imaging cavity case, this operator is the same as the one in the vacuum as no spatial filtering is induced by the cavity. In the regime below threshold considered here, the pump is not depleted, and fluctuations of the pump field do not contribute, at first order to the fluctuations of the signal.

The interaction Hamiltonian of the system, taking into account the thickness of the crystal and the shape of the pump, is given by

$$H_{int}=\frac{i\hbar g}{2l_c}\int_{-l_c/2}^{l_c/2}dz'\int\int d^2x'\{A_P(\mathbf{x}',z')[\hat{B}^{\dagger}(\mathbf{x}',z',t)]^2-\text{H.c.}\}, \quad (4)$$

where g is the coupling constant proportional to the second-order nonlinear susceptibility $\chi^{(2)}$ and $A_P(\mathbf{x}',z')$ the pump field amplitude.

In the following, we will assume that the parametric interaction taking place in the crystal is very weak, which is the case experimentally when cw pump fields on the order of 100 mW are used. In this case, the field amplitude does not vary much in a single pass through the crystal. Therefore, the z dependence of the operators $\hat{a}_l$ can be removed in Eq. (4). The longitudinal variation in the signal operator $\hat{B}$ is then only due to the diffraction inside the crystal, which is fully described by the z dependence of the modal functions $f_l(\mathbf{x},z)$. This is the central assumption of the present paper, which enables us to go beyond the usual thin-crystal approximation.

C. Evolution equation of the field

Using this assumption, we can now investigate the time evolution of the intracavity signal field in the plane C situated in the middle of the crystal ($z=0$) (near-field plane), and of its spatial Fourier transform (far field), taking into account the effects of the crystal thickness and of the finite transverse size of the pump beam.

1. Near-field evolution

In the present case of a weak single-pass variation in the field amplitude inside the crystal, the time evolution of the signal field B in the near-field plane is

$$\frac{\partial\hat{B}}{\partial t}(\mathbf{x},0,t)=-\gamma(1+i\delta)\hat{B}(\mathbf{x},0,t)+g\int\int d^2x''K_{int}(\mathbf{x},\mathbf{x}'')\hat{B}^{\dagger}(\mathbf{x}'',0,t)+\sqrt{2\gamma}\hat{B}_{in}(\mathbf{x},0,t). \quad (5)$$

In this equation, the first term describes the effects of cavity damping and detuning, γ being the cavity escape rate and δ being the normalized cavity detuning. The third term describes the feeding of the cavity through the coupling mirror M_C by the input signal field, $\hat{B}_{in}(\mathbf{x},0,t)$ being the input field operator. We assume here that there is no injected light, so that the input field is in the vacuum state. The second term describes the parametric interaction in the presence of diffraction. In the case of exact collinear phase matching $k_p=2k_s$ and no walk off, the kernel $K_{int}(\mathbf{x},\mathbf{x}'')$ is equal to

$$K_{int}(\mathbf{x},\mathbf{x}'')=A_p\left(\frac{\mathbf{x}+\mathbf{x}''}{2},z=0\right)\Delta(\mathbf{x}-\mathbf{x}''). \quad (6)$$

This kernel appears also in the description of spontaneous parametric down conversion: it is in this case the two-photon wave function of the pair of signal photons generated in the down-conversion process. K_{int} is the product of the pump amplitude in the near-field plane taken at the average transverse position $z=0$ and of a function Δ describing the diffraction effects inside the crystal, equal to

$$\Delta(\mathbf{x})=\frac{ik_s}{4\pi l_c}\int_{-l_c/2}^{l_c/2}\frac{dz'}{z'}e^{(ik_s/4z')|\mathbf{x}|^2}, \quad (7)$$

where $k_s=n_s\omega_s/c$ is the field wave number, and n_s is the index of refraction at frequency ω_s. Δ can be expressed in terms of the integral sine function $\mathrm{Si}(x)=\int_0^x\frac{\sin u}{u}du$,

$$\Delta(\mathbf{x}-\mathbf{x}'')=\frac{k_s}{2\pi l_c}\left[\frac{\pi}{2}-\mathrm{Si}\left(\frac{k_s|\mathbf{x}-\mathbf{x}''|^2}{2l_c}\right)\right]. \quad (8)$$

As expected, in the thin-crystal case ($l_c\to 0$) the function Δ tends to the usual two-dimensional Dirac δ distribution.

In the confocal cavity case, the interaction kernel is the even or the odd part of this one. Indeed, the confocal cavity will filter only the even or the odd part of the spatial modes. The more general coupling kernel of the self-imaging case enables less coupling between modes and therefore twice more transverse modes to be excited.

In the thick-crystal case, the parametric interaction mixes the operators at different points of the transverse plane, over areas of finite extension given by the spatial extension of the kernel K_{int}. This extension is characterized by the width of the sine function, which define a coherence length

$$l_{coh} = \sqrt{\frac{\lambda l_c}{\pi n_s}}. \tag{9}$$

When $|\mathbf{x}-\mathbf{x}''| \gg l_{coh}$, Δ and therefore the kernel K_{int} take negligible values, there is no coupling between these two positions. On the other hand, when $|\mathbf{x}-\mathbf{x}''| \ll l_{coh}$, the coupling mixes the fluctuations. Thus, we can define l_{coh} as the quantum resolution of our system.

Because of the finite size of the pump, the kernel will take negligible values for $\mathbf{x}+\mathbf{x}'' > w_p$. Therefore, we can define the number of transverse modes excited by the parametric process inside the cavity, as the ratio between the size of the pump, and the area defined by l_{coh},

$$b = \frac{w_p^2}{l_{coh}^2}. \tag{10}$$

This definition relies on the classical imaging properties of the system. We will show in the last section of this paper that it is consistent with the computation of the eigenmodes of the system.

2. Far-field evolution

Let us introduce the spatial Fourier transform of the signal field envelope operator [12]

$$\hat{\tilde{B}}(\mathbf{q},z,t) = \int \frac{d^2x}{2\pi} \hat{B}(\mathbf{x},z,t) e^{-i\mathbf{q}\cdot\mathbf{x}}. \tag{11}$$

Equation (5) becomes

$$\frac{\partial \hat{\tilde{B}}}{\partial t}(\mathbf{q},0,t) = -\gamma(1+i\Delta)\hat{\tilde{B}}(\mathbf{q},0,t) + g\int d^2q'' \tilde{K}_{int}(\mathbf{q},\mathbf{q}'')\hat{\tilde{B}}^{\dagger}(\mathbf{q}'',0,t) + \sqrt{2\gamma}\hat{\tilde{B}}_{in}(\mathbf{q},0,t), \tag{12}$$

where the coupling Kernel $\tilde{K}_{int}(\mathbf{q},\mathbf{q}'')$ is the Fourier transform of the kernel (6) with respect to both arguments. Straightforward calculations show that

$$\tilde{K}_{int}(\mathbf{q},\mathbf{q}') = \tilde{A}_p(\mathbf{q}+\mathbf{q}')\mathrm{sinc}\left[\frac{l_c}{2k_s}\left|\frac{\mathbf{q}-\mathbf{q}'}{2}\right|^2\right], \tag{13}$$

where $\tilde{A}_p$ is the spatial Fourier transform of the Gaussian pump profile, i.e., $\tilde{A}_p(\mathbf{q}) = \frac{w_p^2}{2} A_p \exp(-|\mathbf{q}|^2 \frac{w_p^2}{4})$.

The sinc term in the coupling kernel of Eq. (13) is the Fourier transform of the Δ terms in Eq. (6) and correspond to the limited phase-matching bandwidth of the nonlinear crystal. For a thin crystal, phase matching is irrelevant and there is no limitation in the spatial bandwidth of down-converted modes, whereas for a thick crystal, the cone of parametric fluorescence has an aperture limited to a bandwidth of transverse wave vectors $\Delta q \approx 1/l_{coh} \propto 1/\sqrt{\lambda l_c}$. In the self-imaging geometry, the cavity ideally transmits all the Fourier modes, so that the spatial bandwidth is only limited by the phase matching along the crystal. Finally, we have to notice that in the far-field configuration, the $\tilde{A}_p(\mathbf{q}+\mathbf{q}')$ couples different q-vectors modes within the finite width of the pump.

D. Input/output relation

In order to calculate the noise spectrum of the outgoing field, an input/output method is used. The input field is supposed to be in a coherent state and the fluctuations at the output can be inferred. The relation linking the outgoing fields $B^{out}(\mathbf{x},t)$ to the intracavity and input fields at the cavity input/output port [13] is

$$\hat{B}^{out}(\mathbf{x},t) = \sqrt{2\gamma}\hat{B}(\mathbf{x},t) - \hat{B}^{in}(\mathbf{x},t). \tag{14}$$

The evolution equation of the field, either in the near or in the far field, can be solved in the frequency domain by introducing

$$\hat{B}^{in/out}(\mathbf{x},\Omega) = \int \frac{dt}{\sqrt{2\pi}} \hat{B}^{in/out}(\mathbf{x},t) e^{-i\Omega t},$$

which lead to the input/output relation, linking $\hat{B}^{in}(\mathbf{x},\Omega)$ and $\hat{B}^{out}(\mathbf{x},\Omega)$.

In the case of a thin crystal in the near field [8], this relation describes an infinite set of independent optical parametric oscillators. In this case, the squeezing spectrum can be calculated analytically. More generally, this relation in near field links all points in the transverse plane within the coherence area. In order to get the input/output relation, we have to invert the input/output relation by using a numerical method used in [12].

E. Homodyne detection scheme in the near field and far field

In the following sections, we calculate the noise spectrum at the output of the OPO as a function of the detected transverse mode selected by a homodyne detection scheme [14]. By mixing it with a coherent local oscillator (LO) of various shape on a 50% beamsplitter (reflection and transmission coefficients $r = \frac{1}{\sqrt{2}}$ and $t = \frac{1}{\sqrt{2}}$), one can measure the fluctuations on any transverse mode of the output of the self-imaging OPO by measuring the photocurrents difference. The two identical detectors of different size and position are supposed to have a perfect quantum efficiency. All the fields are evaluated at the beam-splitter location, and the z dependence is omitted in the following.

We use two different configurations: near field (x-position basis) and far field (q-vector basis). The complete detection scheme is schematically shown in Fig. 2 and 3. In the near-field configuration, the imaging scheme is composed of a two-lens afocal system (focal length f), which images the

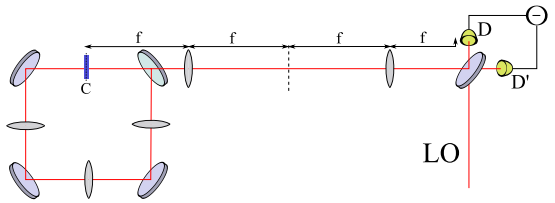

FIG. 2. (Color online) Balanced homodyne detection scheme in the near field. Two matching lenses of focal f are used to image the cavity center C at the detection planes D and D′.

crystal/cavity center plane C onto the detection planes D and D′ (near-field planes). In the far-field configuration, a single lens of focal length f transforms its focal object plane C into the image focal detection plane D. Any image in the object plane C is transformed into its Fourier transform in the plane D (far-field plane).

For near-field imaging, the local oscillator can be expressed as $\alpha_L(\mathbf{x},z)=|\alpha_L(\mathbf{x},z)|e^{i\varphi_L(\mathbf{x},z)}$. The difference photocurrent is a measure of the quadrature operator,

$$\hat{B}_H(\Omega)=\int_{det} d\mathbf{x}[\hat{B}^{out}(\mathbf{x},\Omega)\alpha_L^*(\mathbf{x})+\hat{B}^{out+}(\mathbf{x},-\Omega)\alpha_L(\mathbf{x})], \tag{15}$$

where *det* is the image of the photodetection region at the crystal plane C and assumed to be identical for the two photodetectors. The quantum efficiency of the photodetector is assumed to be equal For far-field imaging, the lens provides a spatial Fourier transform of the output field $\hat{B}_{out}(x,\Omega)$, so that at the location of plane D the field $\hat{B}_D^{out}(x,\Omega)$ is

$$\hat{B}_D^{out}(x,\Omega)=\frac{2\pi}{\lambda f}\hat{\tilde{B}}^{out}\left(\frac{2\pi}{\lambda f}x,\Omega\right). \tag{16}$$

In this plane, $\hat{B}_D^{out}(x,\Omega)$ is mixed with an intense stationary and coherent beam $\alpha_{LO}^D(x)=\frac{2\pi}{\lambda f}\tilde{\alpha}_{LO}(\frac{2\pi x}{\lambda f},\Omega)$, where $\alpha_L(x)$ has a Gaussian shape, with a waist w_{LO}. The homodyne field has thus an expression similar to the near-field case, where functions of x are now replaced by their spatial Fourier transforms,

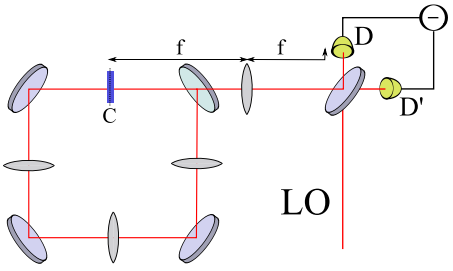

FIG. 3. (Color online) Balanced homodyne detection scheme in the far field. A matching lens of focal f is used to obtain the far-field image of the object plane C at the detection planes D and D′.

$$\hat{B}_H(\Omega)=\int_{det} d\mathbf{q}[\hat{\tilde{B}}^{out}(\mathbf{q},\Omega)\tilde{\alpha}_{LO}^*(\mathbf{q})+\hat{\tilde{B}}^{out+}(\mathbf{q},-\Omega)\tilde{\alpha}_{LO}(\mathbf{q})]. \tag{17}$$

In near and far field, the fluctuations $\delta\hat{E}_H(\Omega)$ of the homodyne field around steady state are characterized by a noise spectrum

$$V(\Omega)=\int_{-\infty}^{+\infty} d\Omega'\langle\delta\hat{E}_H(\Omega)\delta\hat{E}_H(\Omega')\rangle=N+S(\Omega), \tag{18}$$

where $\hat{E}_H$ is normalized so that N gives the mean photon number measured by the detector

$$N=\int_{det} d\mathbf{x}|\alpha_L(x)|^2. \tag{19}$$

N represents the shot-noise level, and S is the normally ordered part of the fluctuation spectrum, which accounts for the excess or decrease in noise with respect to the standard quantum level ($S=0$). One should note that there is a complete equivalence between a setup with a finite and flat local oscillator and infinite detectors and a flat and infinite local oscillator combine with finite-size detectors. We will often use the configuration with finite-size photodetectors in the following.

III. NONCLASSICAL PROPERTIES

We present here the main properties of the fields emitted by the subthreshold self-imaging OPO. We will first consider the squeezing in the near field in a very similar manner as what was done for a confocal OPO. Then we will study the far-field properties and demonstrate local EPR correlations, which did not exist in the confocal case.

A. Squeezing in the near field

As the self-imaging cavity does not exert any spatial filtering on the fields, the nonclassical properties are very similar to those observed in the single-pass configuration. We will here show the main squeezing predictions for such a device, taking into account the thickness of the crystal.

The results of this section are more general than the squeezing properties of the confocal OPO. In fact, the confocal case only allows us to perform homodyne detection with symmetrical detectors. The OPO in a self-imaging cavity allows us to extend these results to any type of detection.

Let us first consider the case of the thin-crystal approximation, where no characteristic length is introduced in the model. We consider a thin-crystal self-imaging OPO pumped by a Gaussian beam. We look at the output quantum fluctuations with a pixel-like detector whose position is varied. In Fig. 4, the squeezing is plotted as a function of the detector distance from the optical axis for different mean powers of the pump ($A_p=1$ corresponding to the threshold on the axis). The squeezing is maximum when the detection is centered on the pump beam and tends to zero far from the center. Figure 4 shows that the squeezing increases with the total

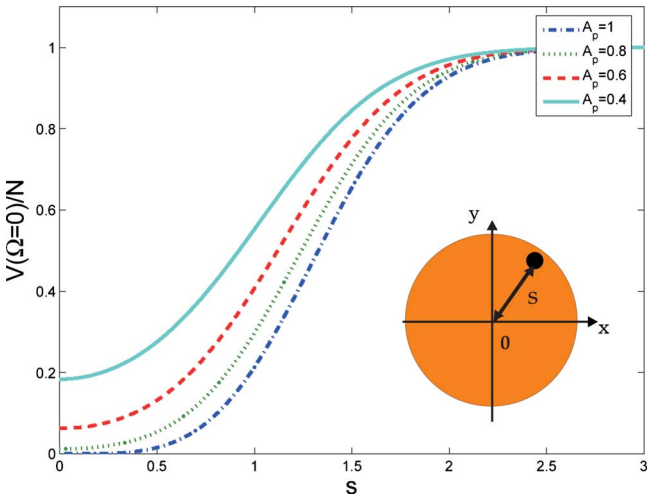

FIG. 4. (Color online) Quantum noise of the squeezed quadrature, normalized to the shot noise at zero frequency and for a pixel-like detector located in the near-field plane, as a function of the pixel distance from the origin s, normalized to the waist of the pump ($s=\frac{\rho}{w_p}$) and for different pump values.

pump power and depends critically on its local value. In the thin-crystal case, the kernel K_{int} depends only on the local pump amplitude and on the transverse coordinate. Hence, any transverse position on the crystal acts as an independent OPO, and the nonclassical properties then only depend on the local pump power at that position.

In a more general realistic study, we have to take into account the finite size of the crystal. For a thick crystal, the coherence length l_{coh} introduced in Eq. (9) has to be taken into account. On transverse size smaller than this coherence length, fluctuations are mixed inside the crystal.

In Fig. 5, we represent the quantum noise as a function of the detector size for different pump waist (normalized to the coherence length). For detectors smaller than the coherence area, the quantum noise goes to shot noise whatever the size of the pump is. As explained in the last paragraph, at that scale the OPO can be considered as locally single mode and

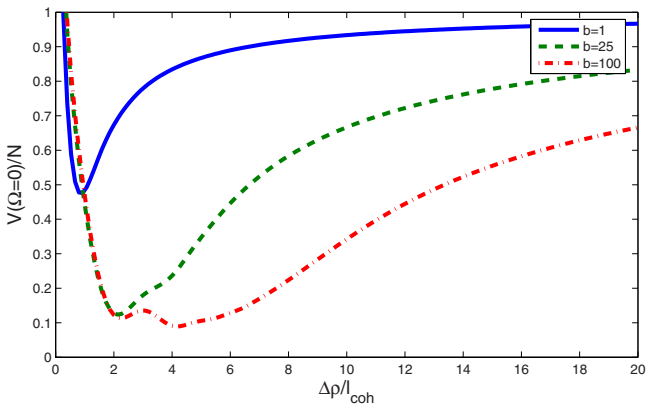

FIG. 5. (Color online) Quantum noise of the squeezed quadrature normalized to the shot noise at zero frequency and in the thick-crystal case, as a function of the radial size of the detector scaled to l_{coh}, plotted for several values of the parameter $b=\frac{w_p^2}{l_{\mathrm{coh}^2}}$.

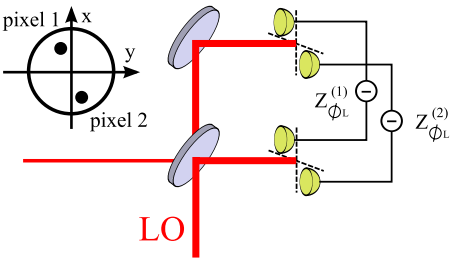

FIG. 6. (Color online) Homodyne detection scheme for the measurement of the quadrature components of the output field on two symmetrical pixels: pixel 1 and pixel 2.

no squeezing can be obtained. For detectors whose size is close the coherence area one, squeezing is obtained. Nevertheless, this squeezing degrades for a given pump waist when the size of the detector increases. For a given pump size, when the detector becomes larger than the excited surface, vacuum fluctuations are coupled to the detected signal and the squeezing degrades. In the same way, for a given detector size, the squeezing decreases with the waist of the pump. In fact, a finite pump size limits the number of excited modes. Increasing the pump size increases the number of excited modes and improves the squeezing.

The graphs correspond to a pump power at threshold. However, the fluctuations never reach zero (corresponding to infinite squeezing) because the measured mode does not match the mode that is perfectly squeezed. Section IV will answer this question, giving the eigenmodes of the system.

B. Entanglement in the far field

In the far field, the analysis has to be performed not in crystal plane (near-field plane) but in its Fourier plane (far-field plane). Squeezing can be observed in the far field when using a symmetrical detector. Indeed, contrary to the near-field case, in the far-field configuration the down-conversion process couples two symmetric k vectors. Thus, in order to recover the squeezing, one needs a symmetric detector relative to the optical axis of the imaging system. The results obtained are therefore the same as those in the confocal cavity, both with a plane pump and with a finite pump. Corresponding calculations are also available upon request to the authors.

The advantage of the self-imaging cavity is that it does not couple the two symmetrical k vectors. Therefore, one expects correlations between two symmetrical areas in the far field, as it will be shown in the following.

In order to characterize the correlation level between symmetrical parts of the beam, we compare the quadrature field fluctuations on two symmetrical pixels. In order to get this quantities, we use the homodyne detection scheme (Fig. 6) proposed in [14], where two symmetrical sets of two detectors measure a quadrature of the field at two symmetrical positions.

Let us consider a pixel-like detector with finite detection area $\Delta\rho_j$; according to Eq. (17) the detected field quadrature is given by

$$\hat{E}^{(j)}_{\phi_L}(\Omega) = \int_{\Delta\rho_j} d\mathbf{q}[\hat{\tilde{B}}^{out}(\mathbf{q},\Omega)|\alpha_L(\mathbf{q})|e^{-i\phi_L} + \hat{\tilde{B}}^{out+}(\mathbf{q},-\Omega)|\alpha_L(\mathbf{q})|e^{i\phi_L}], \quad (20)$$

where we have introduced explicitly the phase of the local oscillator. To compare the fluctuations of the field quadrature measured in two symmetrical pixels $j=1$ and $j=2$, we compare the sum and the difference of these quantities

$$\hat{E}^{(\pm)}_{\phi_L}(\Omega) = \hat{E}^{(1)}_{\phi_L}(\Omega) \pm E^{(2)}_{\phi_L}(\Omega). \quad (21)$$

In order to evaluate the degree of correlation or anticorrelation, we introduce the corresponding fluctuations spectra

$$V^{(\pm)}_{\phi_L}(\Omega) = \int_{-\infty}^{+\infty} d\Omega' \langle \hat{E}^{(\pm)}_{\phi_L}(\Omega)\hat{E}^{(\pm)}_{\phi_L}(\Omega')\rangle. \quad (22)$$

Straightforward calculations show that

$$V^{(-)}_{\phi_L}(\Omega) = V^{(+)}_{\phi_L+\pi/2}(\Omega). \quad (23)$$

It results that the correlation between $\hat{E}^{(1)}_{\phi_L}$ and $\hat{E}^{(2)}_{\phi_L}$ is the same as the anticorrelation between the corresponding orthogonal quadrature components $\hat{E}^{(1)}_{\phi_L+\pi/2}$ and $\hat{E}^{(2)}_{\phi_L+\pi/2}$. In order to calculate Eq. (22), we develop the expression, so as

$$V^{(\pm)}_{\phi_L}(\Omega) = \int_{-\infty}^{+\infty} d\Omega' \langle \hat{E}^{(1)}_{\phi_L}(\Omega)\hat{E}^{(1)}_{\phi_L}(\Omega')\rangle + \int_{-\infty}^{+\infty} d\Omega' \langle \hat{E}^{(2)}_{\phi_L}(\Omega)\hat{E}^{(2)}_{\phi_L}(\Omega')\rangle \pm \int_{-\infty}^{+\infty} d\Omega' \langle \hat{E}^{(1)}_{\phi_L}(\Omega)\hat{E}^{(2)}_{\phi_L}(\Omega')\rangle \pm \int_{-\infty}^{+\infty} d\Omega' \langle \hat{E}^{(2)}_{\phi_L}(\Omega)\hat{E}^{(1)}_{\phi_L}(\Omega')\rangle. \quad (24)$$

The terms $\int_{-\infty}^{+\infty} d\Omega' \langle \hat{E}^{(i)}_{\phi_L}(\Omega)\hat{E}^{(i)}_{\phi_L}(\Omega')\rangle$ correspond to the result of the fluctuation spectra of a homodyne detection scheme using a single pixel. The other terms are cross correlation terms, so that

$$V^{-}_{\phi_L}(\Omega) = V^{+}_{\phi_L+\pi/2}(\Omega). \quad (25)$$

When these variances are below one, EPR beams are obtained at the output of the self-imaging cavity. One should note that these variances correspond to the fluctuation spectrum obtained performing a homodyne detection in the far field with symmetric detectors: the usual connection between squeezing and quantum correlations is exhibited, both side of the same phenomenon [15]. More specifically, the spatial entanglement in the far field arises from the correlations between the modes $\hat{a}_{\mathbf{q}} \sim e^{i\mathbf{q}.\mathbf{x}}$ and $\hat{a}_{-\mathbf{q}} \sim e^{-i\mathbf{q}.\mathbf{x}}$. As $\hat{a}_{\mathbf{q}}$ and $\hat{a}_{-\mathbf{q}}$ are EPR entangled beams, it is well know that the combination of modes

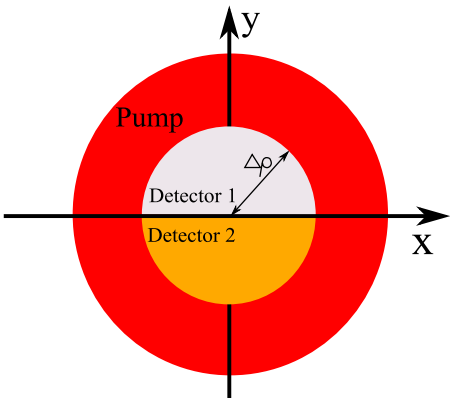

FIG. 7. (Color online) Detection scheme for the inseparability measurement.

$$\frac{\hat{a}_{\mathbf{q}} + \hat{a}_{-\mathbf{q}}}{\sqrt{2}} \sim \cos(\mathbf{q}\,.\,\mathbf{x}),$$

$$\frac{\hat{a}_{\mathbf{q}} - \hat{a}_{-\mathbf{q}}}{\sqrt{2}} \sim \sin(\mathbf{q}\,.\,\mathbf{x}), \quad (26)$$

will be squeezed with respect to two orthogonal quadrature components. The modes proportional to $\cos(\mathbf{q}.\mathbf{x})$ are the even modes: using an even detection scheme, it is possible to see squeezing, as already found in the previous section. Note that if we use an odd detection scheme (symmetrical detectors with an odd local oscillator), it will be also possible to see squeezing in the far field, but on the orthogonal quadrature.

In order to ascertain the inseparable character of this physical state, Duan *et al.* [16] showed that one needs to make two joint correlation measurements on noncommuting observables on the system. They have shown that in the case of Gaussian states, there exists a criterion of separability in terms of the quantity S_{12}, which we will call "separability," and is given by

$$S_{12}(\Omega) = \frac{1}{2}[V^{-}_{\phi_L}(\Omega) + V^{+}_{\phi_L+\pi/2}(\Omega)]. \quad (27)$$

The suddicient Duan criterion for inseparability is given by

$$S_{12}(\Omega) < 1. \quad (28)$$

First, we can perform a joint correlation measurement using two split detectors of same but variable size as depicted in Fig. 7. Figure 8 shows the evolution of the separability at zero frequency $S_{12}(0)=S_{12}$ for different b parameters, in function of the detector radius scaled to $l_{cohf}=\lambda f/2\pi w_p$ [12]. Notice that results are the same as a local squeezing measurement using a circular detector of variable radius $\Delta\rho$ centered on the optical axis.

Figure 9 shows the results obtained in the case of two symmetrical pixels (pixel of size equal to the coherence length l_{cohf}), for different b values, in function of the distance between the two pixels ρ.

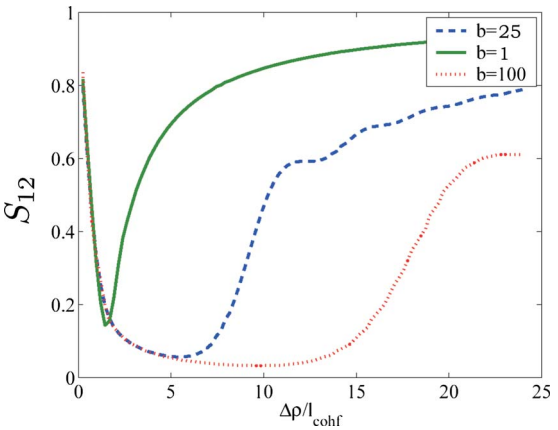

FIG. 8. (Color online) Inseparability at zero frequency, and at resonance, as a function of the radial amplitude of the detector $\Delta\rho$ (scaled to the coherence area l_{cohf}), in the finite pump regime and far-field approach and for different values of b.

IV. PIXEL-BASED MODEL FOR THE SELF-IMAGING OPO

We have so far described the nonclassical properties of the self-imaging OPO using a detection-based geometry, very appropriate to describe actual experiments. One can use another approach based on the spatial properties of the parametric process itself, which gives a different insight into the physics of the system. This powerful technique was first used in [17,18], in the context of bipartite spontaneous parametric down conversion, to characterize and optimize the entanglement between the signal and idler photons using a Schmidt decomposition approach based on the singular value decomposition of the interaction Hamiltonian. The technique has been recently extended by [19] to characterize the quantum properties of a single highly multimode quantum system, namely, the frequency comb generated by a synchronously pumped optical parametric oscillator, made of thousands of different frequency modes around the subharmonic frequency, which cannot be unambiguously separated into two

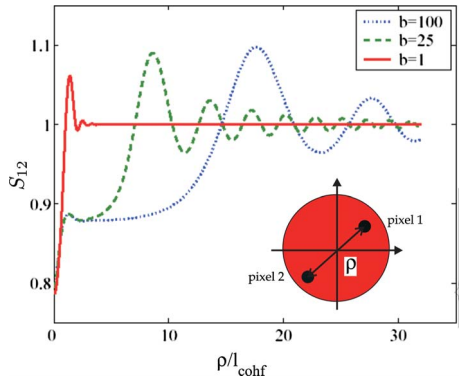

FIG. 9. (Color online) Inseparability at zero frequency, and at resonance, as a function of the distance between the two pixels ρ (scaled to the coherence area l_{cohf}), in the finite pump regime and far-field approach and for different values of b.

parts: the signal modes and idler modes. In this paper, we extend the technique to the case of a multitransverse-mode frequency degenerate OPO.

Let us pixelize the transverse space with pixels much smaller than l_{coh} and develop the OPO equations onto the pixel operators. To simplify the system, we can first consider a one-dimensional pixelization. Let L be the size of the pixelized zone and N be the number of pixels. The pixel i is defined as the zone of size $\frac{L}{N}$ near the abscissa $x_i = i\frac{L}{N}$, with i ranging from $-N/2$ to $N/2$. The pixel operator is therefore

$$\hat{B}_i = \int_{S_i} dx \hat{B}(x). \tag{29}$$

The pixel size must be chosen small enough to ensure the constant value of A_p and K_{int} on every pixel. In this case, the Kernel can be written as

$$K_{int}(i,j) = K_{int}(\mathbf{x}_i, \mathbf{x}_j) \tag{30}$$

and the evolution equation [Eq. (5)] at zero frequency then becomes

$$-\gamma\hat{B}_i + \frac{gL}{N}\sum_j K_{int}(i,j)\hat{B}_j^\dagger + \sqrt{2\gamma}\hat{B}_i^{in} = 0. \tag{31}$$

To solve these N-coupled equations, one must find the eigenvectors and eigenvalues of the symmetric matrix $K_{int}(i,j)$. The K matrix and its spectrum are represented on Fig. 10 in the case of $l_c = 1$ cm and $w_p = 300$ μm. Its diagonalization gives a set of eigenmodes with corresponding eigenvalues. Some of these eigenmodes are represented on Fig. 11; they are very close to a set of Hermite-Gauss polynomials shapes whose characteristic waist is imposed, in our case, by the pump waist.

These modes form a basis of uncorrelated modes of the emitted light. Indeed, let us call $\hat{C}_k$ the eigenmode of eigenvalue λ_k. As $K_{int}(i,j)$ is both self-adjoint and real, λ_k and $\hat{C}_k$ components are all real. In this basis, Eq. (31) can be rewritten as set of equations, one per mode

$$-\gamma\hat{C}_k + \frac{gL}{N}\lambda_k\hat{C}_k^\dagger + \sqrt{2\gamma}\hat{C}_k^{in} = 0. \tag{32}$$

These equations can again be decoupled, using the quadrature operators,

$$\hat{C}_{k+} = \hat{C}_k + \hat{C}_k^\dagger, \tag{33}$$

$$\hat{C}_{k-} = -i(\hat{C}_k - \hat{C}_k^\dagger). \tag{34}$$

The final set of equations is now given by

$$-\gamma\hat{C}_{k+} + \frac{gL}{N}\lambda_k\hat{C}_{k+} + \sqrt{2\gamma}\hat{C}_{k+}^{in} = 0, \tag{35}$$

$$-\gamma\hat{C}_{k-} - \frac{gL}{N}\lambda_k\hat{C}_{k-} + \sqrt{2\gamma}\hat{C}_{k-}^{in} = 0. \tag{36}$$

In this basis, using the input/output relations [Eq. (14)], we can calculate the squeezing properties of the modes $\hat{C}_{k\pm}^{out}$,

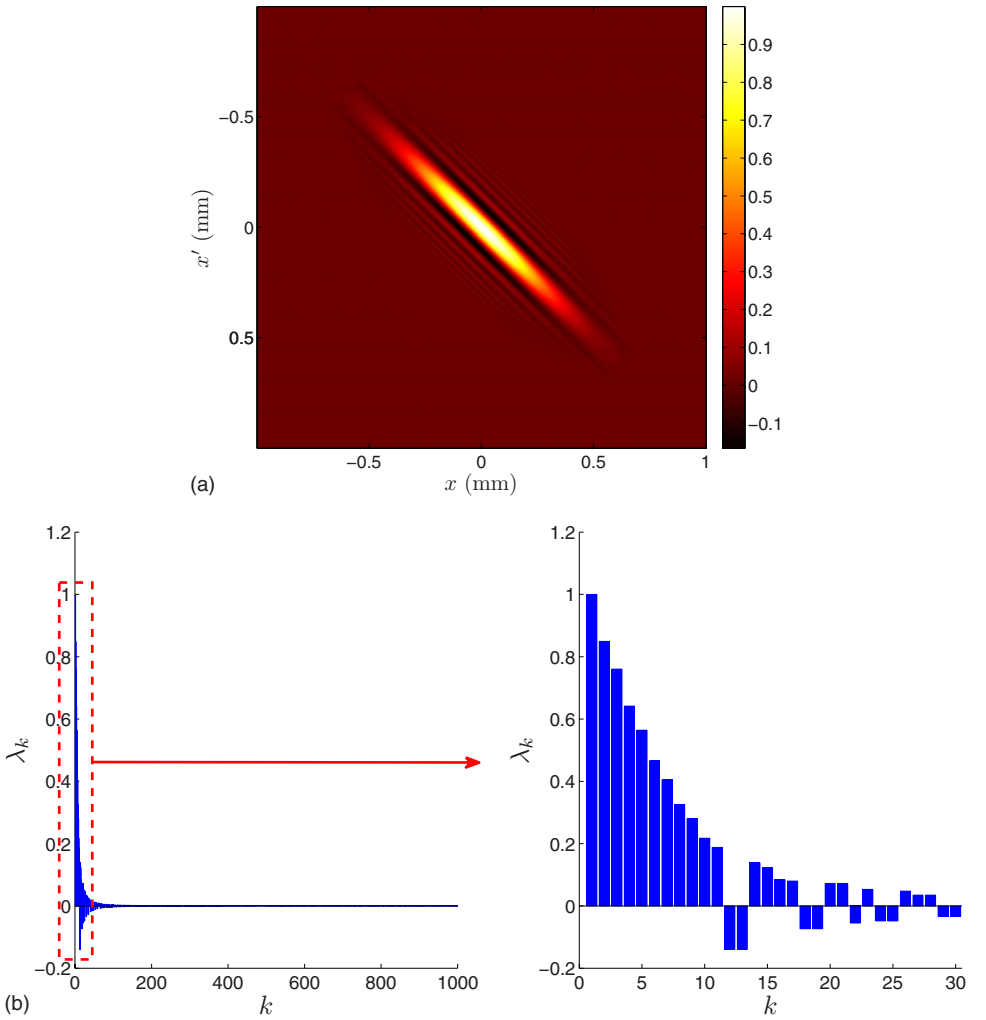

FIG. 10. (Color online) (a) Coupling matrix K_{int} between two points of the crystal. (b) Spectrum of this matrix.

in the near field of the $z=0$ plane. Using the same method as in [19], the fluctuations at zero frequency of the quadratures of the eigenmode $\hat{C}^{out}_{k\pm}$, normalized to the shot-noise level, are given by

$$V_{k\pm} = \Lambda_k^{\pm} = \frac{1 \mp r\frac{\lambda_k}{\lambda_{max}}}{1 \pm r\frac{\lambda_k}{\lambda_{max}}}, \tag{37}$$

where r is the pump power normalized to the threshold and $\lambda_{max}=\max_k \Lambda_k$ is the highest eigenvalue of K_{int}. λ_{max} is of special interest since it is related to the pump power at threshold and C_{max} is the corresponding lasing mode. One can see in the previous equation that for each mode, whose eigenvalue is different from zero, one of its two variances is bellow one, implying that it is nonclassical. However, for eigenvalues very small compared to λ_{max}, the squeezing is negligible. Thus, one can compute the number of relevant mode of the system, for instance, using a threshold eigenvalue (about 10% of the maximum eigenvalue). Another pos-

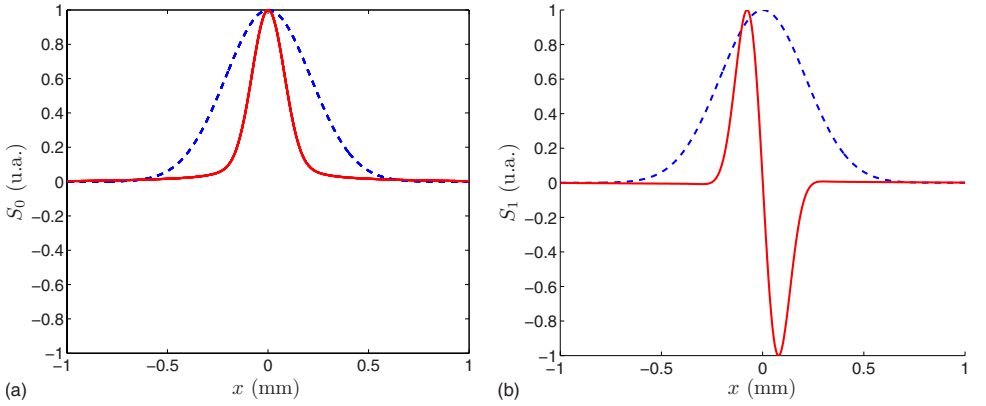

FIG. 11. (Color online) Shape of the two first eigenvectors of matrix K_{int} (red, plain line) for the two highest positive eigenvalues compared to the one of the pump (blue, dotted line).

sibility is to calculate the cooperativity [17] defined from the eigenvalues of the matrix

$$\kappa = \frac{(\Sigma \lambda_k^2)^2}{\Sigma \lambda_k^4}. \tag{38}$$

The obtained number of modes is very close to the one defined in Eq. (10) in a one-dimensional case. For example, using typical experimental values (1-cm-long crystal and a 300 μm pump at 532 nm, which are the values considered on Figs. 10 and 11), we find $b=\frac{w_p}{l_{coh}}=7.5$ and $\kappa=6.8$. This means that in the two-dimensional case, our self-imaging OPO can potentially excite 50 modes.

One should note that from these eigenmodes, it is possible to find the noise properties of the pixel operators B_i^{out} after the cavity, in the near field of the crystal, by inverting the K_{int} matrix, which gives

$$\hat{B}_{i\pm}^{out} = \sum_k V_{ik} \hat{C}_{k\pm}^{out} = \sum_k V_{ik} \Lambda_k^{\pm} \hat{C}_{k\pm}^{in}, \tag{39}$$

$$= \sum_{kj} V_{ik} V_{jk} \Lambda_k^{\pm} \hat{B}_{j\pm}^{in}. \tag{40}$$

If we inject this OPO with an image of any transverse shape, this expression shows that through the decomposition of the input image on the eigenmodes, one can have image amplification.

Using these expressions, we can calculate the measured fluctuations of the quadratures on a detector with an arbitrary shape,

$$V_{det\pm} = \frac{\sum_{ij \in det} \langle \hat{B}_{i\pm}^{out} \hat{B}_{j\pm}^{out} \rangle}{\sum_{i \in det} \langle (\hat{B}_{i\pm}^{out})^2 \rangle}. \tag{41}$$

These numerical simulations show the exact same results as the analytical results presented in Sec. III.

We thus have shown two ways of solving the problem, each having different physical significance. Indeed, in the approach of Sec. III, we have seen that the system has a coherence area that defines the smallest mode having nonclassical properties. This is relevant of quantum imaging applications as it gives which pixel size one can address with quantum techniques. In the present section, we have shown that a proper description of the system consists of an eigenmodes decomposition, modes that have Hermite-Gauss shape and whose squeezing decreases with the mode number. However, these modes shape are complex to measure experimentally.

V. CONCLUSION

In this paper, we have investigated the quantum properties of a self-imaging OPO below threshold. We have shown that it is a more efficient quantum resource than the confocal OPO: it generates a multimode squeezed vacuum both in near-field and far-field configurations, which can be measured using a local oscillator, which is not necessarily symmetric. In addition, the self-imaging OPO generates beams that are EPR entangled in the far field, which is not the case for the confocal OPO. We have outlined the important role of the coherence length l_{coh} of the system, which gives the size of the independently squeezed zones of the transverse plane.

We have also defined and characterized the eigenmodes of the system. This allows us to determine the precise shape of the spatial modes, which are independently and optimally squeezed. Their number is roughly equal to the parameter $b=w_p^2/l_{coh}^2$ encountered in the first part of the paper, which is a kind of Fresnel number setting the number of spatial modes, which can be independently excited in the system.

Self-imaging OPOs are therefore ideal devices to be used in various quantum imaging procedures [2], for example, for parallel quantum information processing of complex images or for the improvement of the extraction of information from images beyond the standard quantum limit.

ACKNOWLEDGMENTS

Laboratoire Kastler-Brossel, of the Ecole Normale Supérieure and the Université Pierre et Marie Curie-Paris 6, is associated with the Centre National de la Recherche Scientifique. We acknowledge the financial support of the Future and Emerging Technologies (FET) program within the Seventh Framework Programme for Research of the European Commission, under the FET-Open grant agreement HIDEAS, Grant No. FP7-ICT-221906.

[1] T. Aoki, N. Takei, H. Yonezawa, K. Wakui, T. Hiraoka, A. Furusawa, and P. van Loock, Phys. Rev. Lett. **91**, 080404 (2003).

[2] *Quantum Imaging*, edited by M. Kolobov (Springer-Verlag, Berlin, 2006).

[3] M. I. Kolobov and C. Fabre, Phys. Rev. Lett. **85**, 3789 (2000).

[4] N. Treps, V. Delaubert, A. Maître, J. M. Courty, and C. Fabre, Phys. Rev. A **71**, 013820 (2005); V. Delaubert, N. Treps, C. Fabre, H.-A. Bachor, and P. Réfrégier, EPL **81**, 44001 (2008).

[5] M. I. Kolobov and L. A. Lugiato, Phys. Rev. A **52**, 4930 (1995).

[6] L. A. Lugiato and Ph. Grangier, J. Opt. Soc. Am. B **14**, 225 (1997).

[7] S. Mancini, A. Gatti, and L. Lugiato, Eur. Phys. J. D **12**, 499 (2000).

[8] K. I. Petsas, A. Gatti, L. Lugiato, and C. Fabre, Eur. Phys. J. D **22**, 501 (2003).

[9] J. A. Arnaud, Appl. Opt. **8**, 189 (1969).

[10] V. Couderc, O. Guy, A. Barthelemy, C. Froehly, and F. Louradour, Opt. Lett. **19**, 1134 (2005).

[11] A. Gatti and L. Lugiato, Phys. Rev. A **52**, 1675 (1995).

[12] L. Lopez, S. Gigan, N. Treps, A. Maître, C. Fabre, and A.

Gatti, Phys. Rev. A **72**, 013806 (2005).
[13] C. W. Gardiner and M. J. Collett, Phys. Rev. A **31**, 3761 (1985).
[14] P. Warszawski, H. M. Wiseman, and H. Mabuchi, Phys. Rev. A **65**, 023802 (2002).
[15] L. A. Lugiato, A. Gatti, and E. Brambilla, J. Opt. B: Quantum Semiclassical Opt. **4**, S176 (2002).
[16] L. M. Duan, G. Giedke, J. I. Cirac, and P. Zoller, Phys. Rev. Lett. **84**, 2722 (2000).
[17] C. K. Law, I. A. Walmsley, and J. H. Eberly, Phys. Rev. Lett. **84**, 5304 (2000).
[18] C. K. Law and J. H. Eberly, Phys. Rev. Lett. **92**, 127903 (2004).
[19] G. J. de Valcarcel, G. Patera, N. Treps, and C. Fabre, Phys. Rev. A **74**, 061801(R) (2006).